Auxetic Dihedral Escher Tessellations

Xiaokang Liu[a], Lin Lu[a,*], Lingxin Cao[a], Oliver Deussen[b], Changhe Tu[a]

[a] *School of Computer Science and Technology, Shandong University, Qingdao, China*
[b] *Computer and Information Science, University of Konstanz, Konstanz, Germany*

Abstract

The auxetic structure demonstrates an unconventional deployable mechanism, expanding in transverse directions while being stretched longitudinally (exhibiting a negative Poisson's ratio). This characteristic offers advantages in diverse fields such as structural engineering, flexible electronics, and medicine. The rotating (semi-)rigid structure, as a typical auxetic structure, has been introduced into the field of computer-aided design because of its well-defined motion patterns. These structures find application as deployable structures in various endeavors aiming to approximate and rapidly fabricate doubly-curved surfaces, thereby mitigating the challenges associated with their production and transportation. Nevertheless, prior designs relying on basic geometric elements primarily concentrate on exploring the inherent nature of the structure and often lack aesthetic appeal. To address this limitation, we propose a novel design and generation method inspired by dihedral Escher tessellations. By introducing a new metric function, we achieve efficient evaluation of shape deployability as well as filtering of tessellations, followed by a two-step deformation and edge-deployability optimization process to ensure compliance with deployability constraints while preserving semantic meanings. Furthermore, we optimize the shape through physical simulation to guarantee deployability in actual manufacturing and control Poisson's ratio to a certain extent. Our method yields structures that are both semantically meaningful and aesthetically pleasing, showcasing promising potential for auxetic applications.

Keywords:
Auxetic structure design, Rotating (semi-)rigid structure, Deployability optimization.

1. Introduction

Auxetic structure are characterized by a property known as negative Poisson's ratio (NPR). Traditional auxetic structures includes re-entrant, chiral, perforated and rotating (semi-)rigid structures. Compared to the first two structures, the rotating structure exhibits more basic shapes and clearer kinematic mode, i.e., each unit rotates around the connection point under external forces, resulting in an expansion effect of the whole structure, as shown in the top row of Figure 1. This characteristic provides a controlled range of properties, making rotating structure versatile for various applications. The perforated structure, on the other hand, can also be regarded as a special type of rotating structure, and researchers can control its mechanical properties by adjusting the slit shape and position.

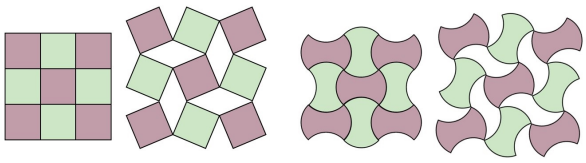

Figure 1: Left is a rotating (semi-)rigid structure based on squares, and right is a rotating structure based on simply designed squares.

In recent years, with advances in materials science and

*Corresponding author:
Email address: llu@sdu.edu.cn (Lin Lu)

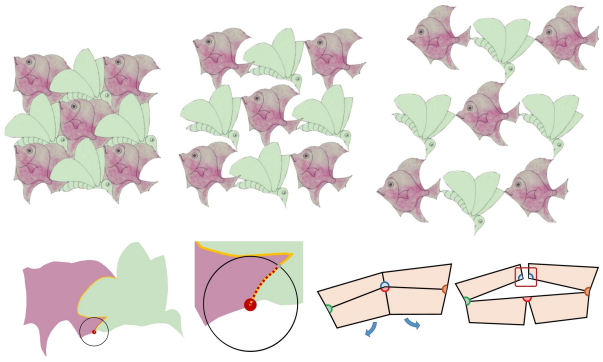

Figure 2: Top row: a failed case to deploy a "fish and butterfly" dihedral tessellation. Bottom row: two challenges for rotational deployable structures: 1) features that express the meaning of the shape may hinder the rotation process when the basic units are deployed; 2) the frame formed by the hinge points connected between the units is not a regular shape and may not remain connected after deployment.

digital fabrication, attention has been poured into creative design explorations based on easily controllable rotating (semi-)rigid structures. From the investigation of the properties of different rotational structures based on various polygons [1, 2, 3, 4, 5, 6, 7, 8] to the generation of a variety of customized complex 2D structures [9, 10] and 3D surfaces [11, 12, 13, 14, 15] based on designed rotating (semi-)rigid structures.

However, these structures often rely on the rotation of basic geometric elements, such as parallelograms and rhombuses, which also present significant design opportunities, particularly in the realm of custom design and manufacturing.

This paper delves into the exploration of introducing meaningful contours to the fundamental units of rotating structures, enhancing their visual appeal and creating a sense of intuitive aesthetics. Specifically, we aim to characterize these structures in their compact state as dihedral Escher tessellations, where the intricate patterns, symmetries, and dual figure-ground arrangements evoke fascination and challenge conventional visual perception and categorization. By incorporating these captivating patterns into the compact form of auxetic structures, we not only enhance their aesthetic value but also explore the fascinating interplay between form and perception.

This introduces two primary challenges. Firstly, significant features of the input shapes may impede the smooth rotation process when the basic units are deployed. Secondly, the frame formed by the connections between the units may deviate from regularity, potentially leading to issues with deployment and maintaining structural integrity, as shown in Figure 2. Overcoming these challenges necessitates the development of novel methods to optimize the profile of these structures. This optimization process involves leveraging a metric function that takes into account both the rotational degrees of freedom and shape semantics. The goal is to strike a delicate balance between aesthetic appeal and deployability.

Our algorithm takes as input a given dihedral Escher tessellation or a single shape (calculating its corresponding dihedral tessellation) and conducts deformation optimizations based on this tessellation. Then we deform and optimise the contour using the aforementioned metric function to generate a manufacturable shape with practical utility.

Our contributions can be summarized as follows.

- We introduce the concept of auxetic dihedral tessellation based on rotating (semi-)rigid structure with clear unit shapes, which can be deployed into a target developable surface through actuation.
- We propose an algorithm and a corresponding framework that deform given dual shapes to create a deployable dihedral Escher tessellation.
- We define a deployability metric function for this rotational structure and propose a deployability optimisation method based on this function.

2. Related Work

2.1. Auxetic Structures

Traditional auxetic mechanical structures comprise many different types including re-entrant structures [16], chiral structures [17, 18], rotating (semi-)rigid structures [1] and perforated structures [19]. Grima et al. [1, 2, 3, 4, 5, 6, 8] explored different kinds of rotational structures based on various polygons, conducted a theoretical analyses and discussed the relationship between different deployment methods, structural parameters and corresponding metamaterial properties. Choi et al. [9] proposed an inverse design framework to generate a compact reconfigurable and rigid deployable Kirigami patterns for a given

a target shape. Warisaya et al. [10] provided topological variations of corner-connected kinematic tiling to generate novel auxetic structure based on irregular and aperiodic rhombic tiles. Attard [20] and Li et al. [21] explored meta-materials composed of three-dimensional units and the resulting material properties. Gatt et al. [22] extended hierarchical rotating structure in order to obtain additional benefits of a hierarchy while retaining the properties of a negative Poisson's ratio.

Grima et al. [19, 23] extended rotating rigid units into perforated structures using a similar mechanism, containing diamond, star or triangular-shaped perforated sheets that exhibit auxetic behaviour for tension and compression. Slann et al. [24], Pagliocca et al. [25] and Morvaridi et al. [26] explored the influence of various parameters of the perforations on the properties of the material. Mizzi et al. [27], Shan et al. [28] introduced slit perforations within sheets/blocks of the material and adapted the parameters of the slits to create auxetic systems with different behavior.

2.2. Deployable Surface

In the last few years, the focus of research has shifted to inverse design optimization approaches which transform or assemble fabricated components to produce a target design surface. This is a very interesting but simultaneously challenging computational problem, since its solution usually depends heavily on the material behavior of the individual components and the way how they are connected together to form a flexible and deployable structure.

Konakovic [11, 12] and Jiang et al. [13] developed novel deployable structures that can be deployed from two-dimensional flat sheets, using slits or perforations, to three-dimensional shapes via inflation or gravitational loading. Inspired by ancient geometric motifs, Rafsanjani et al. [14] proposed bistable mechanical meta-materials that exhibit auxeticity and are able to keep stable in a specific deployment. Chen et al. [15] improved Rafsanjani's work by enabling bistable structures to be deployed into 3D surfaces. Schüller et al. [29] innovatively introduced the concept of a "zipper," which can rapidly form a target 3D object by zipping up the boundaries. Ren et al. [30] proposed an optimization-based method to generate planar curved ribbons to weave smooth freeform geometric shapes.

In beam structure research, Panetta et al. [31] introduced the "x-shell," an assembly of elastic deployable beams with rotational joints. Pillwein et al. later developed the elastic geodesic grid structure for easy-to-fabricate bent lamellas from a planar setup [32]. They enhanced this with patch-based grids for high local curvature features [33] and computational methods for planarity [34]. Jiang et al. [35] and Liu et al. [36] delved into quadrilateral grids for freeform buildings. Other innovations include deployable scissor linkages [37] and umbrella meshes [38] to approximate diverse freeform shapes.

The above work has mainly focused on calculating the ability to approximate surfaces of the whole structure and its kinematic mechanism, without considering adding shapes with aesthetic properties to the structure.

2.3. Traditional Escher Tessellations

In recent decades, tessellations have become pivotal in artistic expression, comprising repeating shapes without gaps or overlaps. Notably, Dutch artist and mathematician M.C. Escher's works—distinguished by intricate patterns, symmetries, and dual figure-ground compositions—have profoundly influenced the field [39]. His creations highlight visual perception ambiguities, intriguing computer graphics enthusiasts.

Dress [40] presented a class of dihedral Escher tilings, "Heaven and Hell patterns," while Grünbaum and Shephard [41] outlined the underlying mathematics. Kaplan and Salesin [42] coined "Escherization" in computer graphics and later detailed a method for "dihedral Escherization" [43]. Koizumi and Sugihara [44] approached Escher tiling as a maximum eigenvalue problem. In contrast, Ono et al. [45] used genetic algorithms for shape optimization. Nagata and Imahori [46] integrated an energy function with an as-rigid-as-possible (ARAP) deformation scheme. Dual shape Escher tilings [47] focused on enhancing shape perception, and Lin et al. [48] combined matching and warping for Escher-like transformations.

Fabricable Escher tiles aim at being assembled practically: Yen and Séquin [49] devised a method for Escher tiling on a spherical domain. Howison and Séquin [50] explored 2.5D isohedral tilings via extrusion and mesh editing and crafted 3D versions using predefined lattices. Similarly, Liu et al. [51] generated printable tiles, leveraging solid and void areas. Unlike these studies that focus

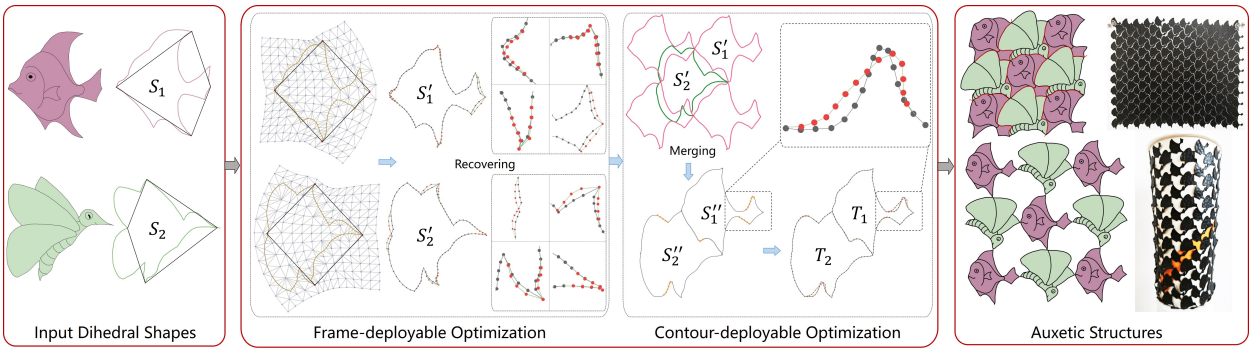

Figure 3: Starting with the dual shapes of a dihedral tessellation, we first deform them separately using a two-step ARAP-based deformation method to transform their anchor frames into a regular geometric unit (here a rhombus). Then, we merge the two shapes and perform a deployability optimisation based on a deployability metric function to obtain the final deployable dihedral Escher tessellation.

solely on shape constraints, our work also addresses the rotational freedom during deployment.

3. Overview

The auxetic dihedral Escher tessellation generation problem can be formulated as follows. Given target close patterns S_1 and S_2, we compute T_1 and T_2, so that:

1. T_1, T_2 are "mutual surrounded", and can tile the entire plane without any gap or overlap;
2. T_1, T_2 can rotate and expand without obstructing each other;
3. T_1, T_2 and S_1, S_2 are as similar as possible.

The first two constraints ensure that the target structure can be driven to expand from a closed, undeployed state in the plane to a deployed state. The third one ensures that the result retains the contour features of the target shapes, preserving their aesthetic and interesting properties.

The *mutual surroundings constraint* [51] refers that each unit is surrounded by units of the other type and only connect to its own kind through four points. To facilitate the description of the whole algorithmic process, these four connecting points of one unit are termed as *anchor points*, and the frame formed by these points is called the *anchor frame*. In this paper, the anchor frame is limited to a quadrilateral since it have more segments and designing freedom to fit complex input patterns with less deformation than triangles.

To ensure that the meaningful shapes rotate without obstructing and the entire structure can deploy under the forces on the sides, our structure must adhere to the "*deployable constraints*", including *frame-deployable constraint* and *contour-deployable constraint*.

The *frame-deployable constraint* mandates that each shape's anchor frame be regular, such as a parallelogram, rectangle, rhombus, or square. In rotating structures, for successful expansion at a four-unit intersection, the sum angles of adjacent anchor frames must total 180°. Non-compliance risks deployment issues or fractures due to alignment conflicts, as shown in Figure 2. Given the shape's periodicity, the anchor frame should at least be a parallelogram.

The other is *contour-deployable constraint*. The anchor points divide the contour into four segments, and based on the kinematic motion of our structure, we can infer that adjacent shapes deploy around a shared rotation axis (anchor point) from their shared edge segment. For a point on a segment, its rotating path is a circle centered on the axis of rotation with the distance between this point and the circle center as the radius. If there are two or more intersections between this path and the edge segment, it indicates that on the forward rotational path of this point, there exists points of a neighboring unit, and they will obstruct each other. Thus, the contour-deployable constraint requires that on the forward path of each point on edge segment, there are only points belonging to the same unit, so that to ensure unobstructed rotation.

Based on the above constraints, we design a deploya-

bility metric function and a pipeline for the generation of the auxetic structure as shown in Figure 3. Our algorithm takes an existing Escher dihedral tessellation consisting of two shapes, denoted as S_1 and S_2, as the input. Alternatively, one can also input a single pattern and then employ the algorithm described in [51] to generate an initial dihedral Escher tessellation as the input. Subsequently, we employ a two-step deformation optimization process for the dual shapes S_1 and S_2. Firstly, we deform them using the ARAP (as-rigid-as-possible) method [52] to ensure that their anchor frames are deformed to fit a regular template. Next, we merge the two shapes and perform deployability optimization based on our deployability metric. This optimization process allows us to obtain the final dual shapes, denoted as T_1 and T_2.

4. Technical Details

In this section, we will sequentially introduce our deployability metric function and the subsequent steps of deforming and optimizing based on this function in detail.

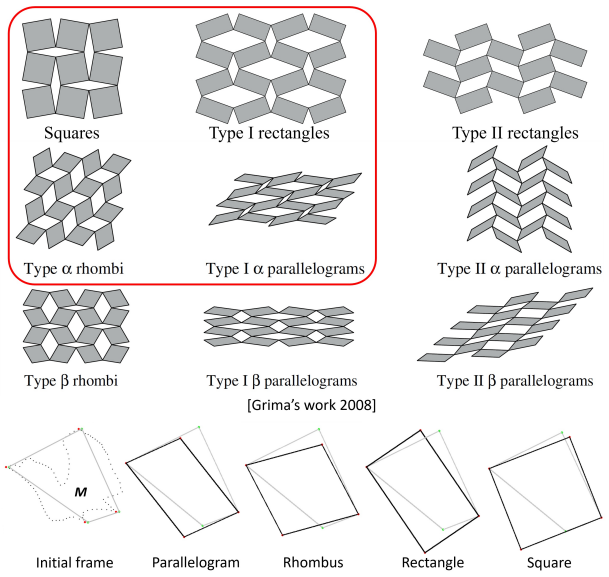

Figure 4: Based on [6], we choose four feasible templates and their corresponding deploying ways for our project, then calculate the error between the target framework and these template, and choose the one with smallest error.

Beforehand, anchor points are initialized according to the arrangement of the two types of shapes in the input dihedral Escher tessellation. Each shape is represented by a point set with $\mathcal{N}$ points (in this paper, $\mathcal{N}$ is 100), where the points connecting each shape to its four counterparts are noted as anchor points. Once the anchor points are determined, the subsequent distance calculation is also determined.

4.1. Deployability Metric

Our deployability metric consists of two components, frame-deployable distance (FDD) and contour-deployable distance (CDD), corresponding to the frame-deployable constraint and the contour-deployable constraint, respectively.

Frame-deployable distance (FDD). FDD describes the minimum distance between the anchor frame and the regular deployable template. Based on the previous definitions, it is known that only if the anchor frame is a regular geometric shape, can such rotating (semi-)rigid structures be ensured to deploy without obstruction, deformation, or buckling. Therefore, the FDD is defined as the minimum consumption required to deform the current irregular anchor frame to a regular shape.

Grima et al. [6] introduced nine deploying methods for four types of regular units. Type I systems have the characteristic of always having a rhombus-shaped empty area between the shape units, while Type II systems do not. The α-type represents a system made from rhombus having their smaller angle attached with the larger angle of adjacent rhombus, while the β-type represents a system with rhombus having their smaller angle attached with the smaller angle of adjacent rhombus and the larger angle being attached with the larger angle.

It is worth noting that in Type II structures, when they are in a tightly contracted state, the long edge of the unit is always aligned with a short edge and a portion of another long edge. The high degree of coupling of the boundaries makes it difficult to design shapes for the units of a structure with such kinematic mode. Type β structures do not achieve a fully tiled state when they are undeployed. Therefore, four types of geometric elements, squares, rectangles, rectangles and parallelograms, and their corresponding four deploying methods are retained as the deployable templates for this paper, as shown in red box in Figure 4.

For a pattern S, FDD(S) describes the minimum distance between its anchor frame S^f, and the regular geometric template, whose shape parameters needs to be calculated first. Here we will introduce how to determine a corresponding template shape S^t for a given template type by controlling the anchor point movement:

1. Parallelogram: fix one pair of relative anchor points and move another pair of relative anchor points so that the diagonals are equal to each other.

2. Rhombus: rotate the diagonals so that they are perpendicular to each other.

3. Rectangle: extend the short diagonal so that it is equal to the other one.

4. Square: do not require additional calculations.

Then, we use Procrustes analysis to align four different templates with anchor frame S^f respectively. Procrustes analysis is a common tool in statistics and shape analysis to align shapes by means of translation, scaling, and rotation. For a shape composed of $(p_1, p_2, ...p_N)$, first aligned with another shape's centroid by translating its centroid $\overline{p}$. The two shapes are then scaled so that the **root mean square distance** $s = \sqrt{\frac{\sum_{i=1}^{N}(p_i-\overline{p})^2}{N}}$ is equal. When rotating, one shape is fixed as the reference direction, the other shape is rotated around the center of mass, and then traverse all angles to find the optimal rotation angle that minimizes the sum of the squared distances (Euclidean distances) between the corresponding points. The minimum value can be used as a statistical measure of the difference between the two shapes, often also referred to as Procrustes distance (PD) :

$$PD(A, B) = \sqrt{\sum_{i=1}^{N} |p_{Ai} - p_{Bi}|^2} \tag{1}$$

We calculates the PD between four template shapes and anchor frame and find the most similar template S^t_{min} with minimum PD. Then the ratio of the PD(S^f, S^t_{min}) to the perimeter of S^f is denoted as FDD(S):

$$FDD(S) = \frac{PD(S^f, S^t_{min})}{Perimeter(S^f)} \tag{2}$$

Contour-deployable distance (CDD). CDD describes the minimum consumption required to optimize an arbitrary contour to be deployable. If a contour shape is defined as *deployable*, then the rotation path of each point on the edge segment just have one intersection with this segment, otherwise the unit will inevitably be obstructed with neighboring unit during deploying. As shown in the left of Figure 5, the gray areas of two adjacent units obstruct each other from rotating.

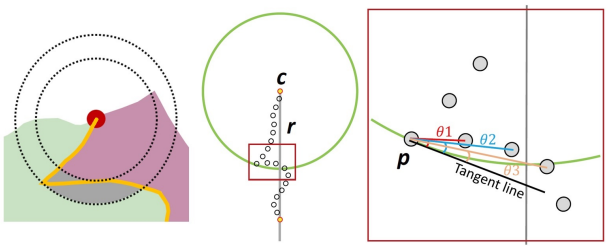

Figure 5: As the edge rotates around center c, point p moves along the green path, which is the circle centered at c with a radius r. There are three points that collide with p. We calculate in turn the angle of their connecting line to the tangent line at point p and regard the sum of the angles of all pairs of collided points as the deployability of this edge.

The area of the grey can reflect the consumption of optimizing a shape into a deployable to a certain extent, but sometimes different shapes having the same area face completely different optimization difficulties. Therefore, in this paper, we consider evaluating the consumption of optimization through the geometric positional relationship of points.

As shown in Figure 5, for each point p_i on the edge, check if there is an **obstructed point** $p_{i+t}, t > 0$ within the circular rotation path of p_i, and if so, compute the angle $\theta_{(i,i+t)} < 90°$ between the line segment $p_i p_{i+t}$ and the tangent line of p_i. The p in the case shown in Figure 5 has three obstructed points. Calculate the corresponding angles of these three points, and the sum is denoted as the contour-deployable distance of point p. Subsequently, the entire edge is traversed and the value of all points is computed to obtain the contour-deployable distance of the edge e. Since the contour of shape S is divided into four segments by four anchor points, the CDD(S) can be further defined as:

$$CDD(S) = \sum_{j=1}^{4} \sum_{i=1}^{N_{e_j}} \sum_{k=1}^{N_{p_i}} \frac{|\theta_k|}{\pi N_{p_i}} \tag{3}$$

Here, N_{p_i} is the number of obstruction points encountered by point p_i, θ_k is the angle between the line connecting p_i and the kth obstruction point and the tangent line, and N_{e_j}

denotes the number of points on side e_j.

Based on the above two metrics, we can obtain the deployability score $DepDis$ for shape S as:

$$DepDis(S) = FDD(S) + CDD(S) \tag{4}$$

Note that the computation of $DepDis$ depends on the position of the anchor points which are determined as the dihedral tessellation is input. Therefore, when there is a large number of inputs, we can perform a quick filtering of the input dihedral shapes with the help of the Equation 4. In addition, a difference in the direction of rotation changes the position of the center of the circle, resulting in a change in the rotation path, which in turn affects the calculation of the contour-deployable distance. Users can specify the direction of rotation for one type of shapes.

4.2. Deployable Optimization

In this section, a two-step optimization approach is employed to optimize shapes S_1 and S_2 respectively by minimizing their $DepDis(*)$, which consists of two components: $FDD(*)$ and $CDD(*)$. Firstly, S is deformed such that its anchor frame S^f is simultaneously deformed into a specific template S^t_{min}. Subsequently, the deformed S' undergoes a local contour optimization to obtain final shape T satisfying the contour-deployable constraint.

Optimizing frame-depolyable distance: This step aims to align the anchor frame S^f with the template S^t_{min} by deformation. However, only the target positions of the four anchor points are known, making it hard to deduce the complete deformed contour shape based on the movements of anchor points and the original geometric information of the contour. Traditional deformation methods rarely succeed in accurately transforming the anchor frame into the target template while preserving the contour features as much as possible. To address this issue, we proposes a bounding box-based As-Rigid-As-Possible (ARAP) method to deform the anchor frame. The ARAP method [52] utilizes a point cloud representation and operates on a triangular mesh generated by triangulating points within the contour, ensuring a global shape consistency that mimics the behavior of real objects under deformation, the results are shown in Figure 6-(b).

However, deforming such a mesh by moving the anchor points usually leads to issues, as shown in the green box in Figure 6-(b): triangles near the anchor points undergo significant changes, while internal triangles change very little. This may result in severe distortion or deformation of contour features and, in some cases, even lead to overlapping triangles. While this method achieves satisfactory overall shape deformation, there is still room for improvement in preserving the features of contours, for this reason, the concept of bounding box-based ARAP is introduced.

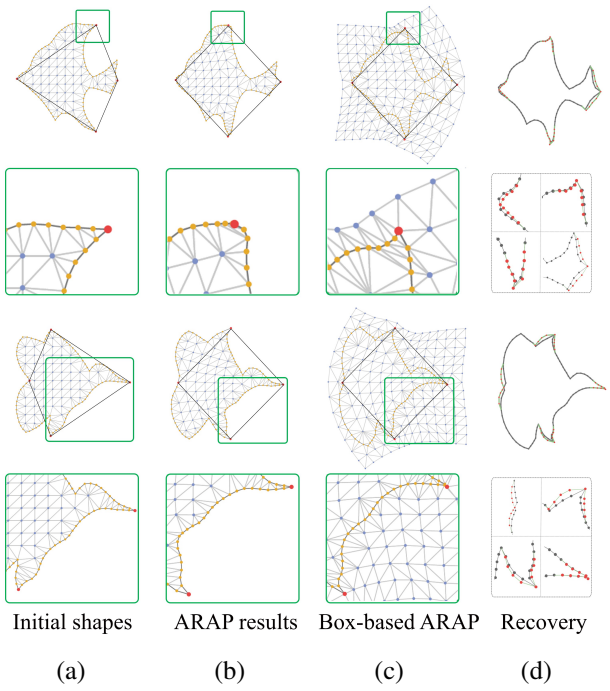

Figure 6: Column (a) shows a triangulation after adding points within the contour; column (b) shows the results after applying ARAP deformation; (c) shows a triangulation obtained by scattering points within a bounding box, and its deformation result using ARAP; and (d) shows S' after boundary recovering.

Different from the typical bounding box determined by the minimum and maximum x and y coordinates, the bounding box used here is expanded outward, leaving a margin width of w_{margin} on all sides. Then triangulate all points including the original contour points and the points scattered in the entire bounding box. Subsequently, the ARAP algorithm is performed and the result is shown in Figure 6-(c).

In comparison to the results in Figure 6-(b), anchor

points in the upper green box in Figure 6-(c) still maintain angles after movement without collapsing inward, and in the lower green box, the butterfly's abdomen no longer collapses inward as before. This indicates that the triangles outside the contour within the bounding box act similarly to supports, and the deformation component suffered by the anchor point spreads to the nearby triangles, thus reducing the distortion.

To further preserve the features near anchor points, we propose a boundary recovery method to recover the geometric features around the anchor point, through the local geometric information near the anchor points, as shown in Figure 6-(d). Firstly, the angles $\angle p_{i-t}p_ip_{i+t}, t \in [1, t_{max}]$ between the anchor point p_i and the adjacent points p_{i-t} and p_{i+t} on both sides are calculated and recorded before deformation. Here, we recommend setting t_{max} as $0.05 * \mathcal{N}$. Based on the difference and direction of the angles before and after the deformation, as well as the Euclidean distance between pairs of points, the points on both side are rotated around the anchor point and translates to the new position. This two-step approach allows for more precise control over the deformation from S_1, S_2 to S'_1, S'_2 with better visual appearance.

Optimizing contour-deployable distance: This step aims to deform the dual shapes so that they do not obstruct each other when deployed. Before optimization, S'_1 and S'_2, the results of frame-deployability optimization for S_1 and S_2, are supposed to be merged. The merged shape S''_1, S''_2 can be calculated by the interpolation function:

$$\mathcal{S}(M) = \lambda * \mathcal{S}(A) + (1 - \lambda) * \mathcal{S}(B) \tag{5}$$

$\mathcal{S}(*)$ represents an contour composed of an ordered set of points, λ is used to adjust the interpolation weight of shape A and B.

This merging process is illustrated in Figure 7: the anchors of the two shapes are aligned, and the remaining points between two anchor points are always in one-to-one correspondence, and then the positions of the merged points are calculated according to the above Equation 5. The general merged result is S''_1, and the dual shape S''_2 is obtained by recombining the four edges.

To find a proper λ that makes the merged result S''_1 and S''_2 to be as similar as possible to the initial shape S_1 and S_2, we use the following function to measure the similarity between two shapes:

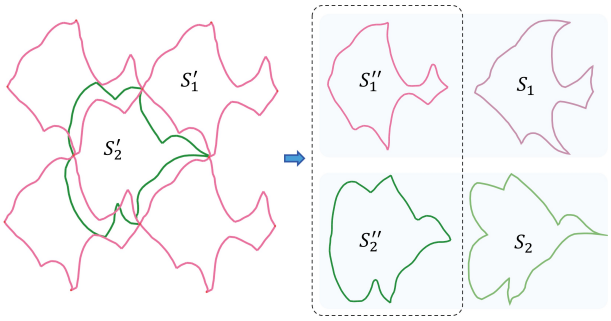

Figure 7: Shape merging: S'_1 and S'_2 are merged to obtain the interpolated shapes S''_1 and S''_2.

$$Sim(A, B) = \phi(A, B) + \omega(A, B) + Insec(A, B). \tag{6}$$

Here, $\phi(A, B)$ is a shape similarity function based on TAR descriptors, which is introduced in [53]. $\omega(A, B)$ is the area function defined as:

$$\omega(A, B) = Area(A \cap B)/Area(A \cup B). \tag{7}$$

The last item $Insec(A, B)$ is a penalty score to penalize self-intersections in A or B, and the more severe the self-intersections, the lower this value will be in the range [0,1]. We can see that the larger $Sim(A, B)$ is, the higher the similarity between the shapes. Therefore, we would like to find a λ_{max} to maximize the following equation:

$$E_{sim} = \min(Sim(S_1, S''_1), Sim(S2, S''_2)) \tag{8}$$

When $\lambda = \lambda_{max}$, S''_1 and S''_2 will obtain highest similarity with S_1 and S_2.

After merging, we provide a deployability optimisation method to ensure that the dual shapes satisfy the contour-deployable constraint.

Based on the Equation 3, to minimize the $CDD(S)$, we adopt an iterative method for deployability optimization, as illustrated in Figure 8. For each edge of the shape, we check each obstructive pair $CP^0_i(p_{il}, p_{ir})$ of points p_{il} and p_{ir} on the edge, calculate the angle θ_i between their connecting line and the tangent line at p_{il}, then rotate this pair CP^0_i around its midpoint in the direction that decreases the θ_i (clockwise in the Figure 8) for $\alpha_0 * \theta_i$, $\alpha_0 = 0.5$. Then, we rotate the neighbour pairs $CP^t_i(p_{il-t}, p_{ir+t})$ of

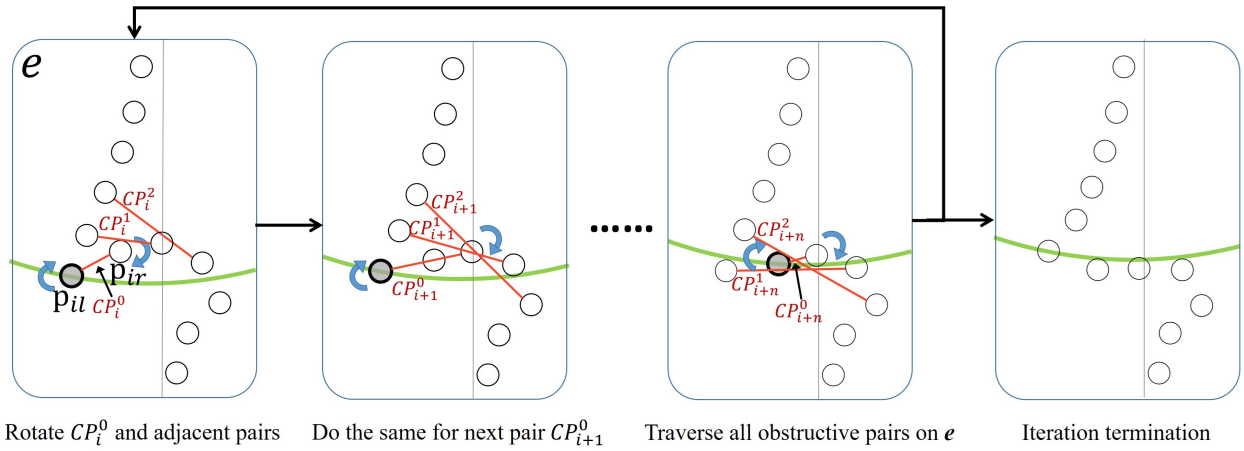

Figure 8: We detect each collided pair $CP_i(p_{il}, p_{ir})$ of points p_{il} and p_{ir}, calculate the angle θ_i between their connecting line and the tangent line at p_{il}, then rotate this pair CP_i and its neighbour pairs $CP_{i+t}(p_{il-t}, p_{ir+t})$ around each pair's medial point for a certain angle $\alpha_t * \theta_i$, and α_t decreases as t increases. The algorithm stops when there are no more colliding points on the edge or the number of iterations reaches the upper limit

CP_i^0 around each pair's medial point for a certain angle $\alpha_t * \theta_i$, where $t \in [0, t_{max}]$, $\alpha_t = \alpha_0/(t+1)^2$ and here $t_{max} = 0.05 * \mathcal{N}$.

Traverse and optimize all the obstructing point pairs CP_{i+n}^0 on the edge and their neighborhoods, and perform the next iteration after the traversal is completed until the number of iterations reaches a predetermined threshold or there are no more obstructive point pairs on the contour.

Note that only optimizing the obstructive point pair CP_i^0 leads to significant cuts or distortions on the contour, so even if the neighboring point pairs $CP_i^t(p_{il-t}, p_{ir+t})$ are not obstructing each other, the algorithm still rotates them so as to ensure the contour to be smooth. On the other hand, when FDD is optimized, the anchor frame will morph into a template and the anchor points will not move again. At this point, a new contradiction arises: if the optimized point pairs are close to the anchor points, the optimization process will rotate the fixed anchor points; if the anchor points are completely fixed and only the other points are moved, it will also lead to severe cuts near the anchor points. To solve this problem, our algorithm further restricts the rotation range of the points near the anchor point based on their distance, i.e., the angle of rotation at each optimization is preceded by the coefficient $\Delta index/n_e$, and $\Delta index$ is the subscripted distance from this point to the anchor point.

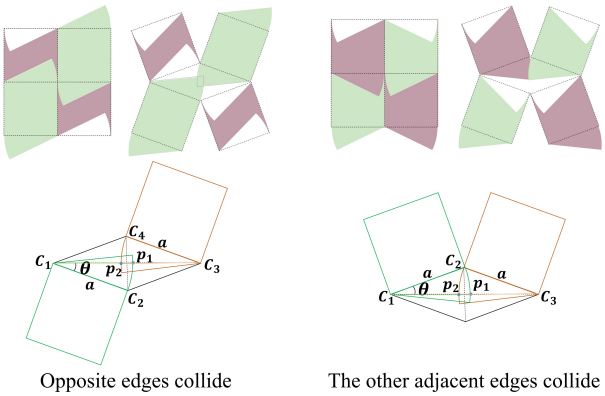

Figure 9: Non-adjacent edges will also be collided.

4.3. Non-adjacent Edge Deployable Optimization

The shape deployability metric function utilized in this paper has been previously introduced. However, this metric function takes into account the degrees of rotational freedom when rotating the units around the axis, which means it only takes into account the deployability optimization of adjacent edges. When deploying our structure, obstructive situations may arise on the other side of neighboring edges or even opposite edges, as illustrated in the top row in Figure 9.

To detect potential collisions among these edges, the

method described in the bottom row of Figure 9 are employed. For the case of opposite edges, when the rota-tion angle θ gradually increases from zero as the units deploy, it can be guaranteed that no collision will oc-cur if $length(C_1\,p_1) + length(C_3\,p_2)$ is always smaller than the $length(C_1C_3)$, i.e., $length(C_1\,p_1) + length(C_3\,p_2) < 2a\cos\theta$, here C_1, C_3 are rotation axis, and p_1, p_2 are the intersections of the line (C_1C_3) and the two units. Similarly, for the case of the other adjacent edges, $length(C_1\,p_1) + length(C_3\,p_2) < 2a\cos\theta$ is what we expect.

It is a natural consideration to include all possible obstructing edge pairs in the contour-deployability constraint optimization framework of this chapter. However, these non-adjacent two edges are optimized independently of each other, and only after determining the state of both edges can we know exactly whether there will be an obstacle or not. It is therefore difficult to optimize simultaneously to ensure that nearly no shape features are lost and exactly no collisions occur. We design a visual UI which is an intuitive solution to optimize these edges in real time as well as to better preserve the boundary features.

4.4. NPR properties analysis

The Poisson's ratio is the ratio of the transverse positive strain to the axial positive strain in a material subjected to unidirectional tension or compression, and is an inherent property of the material itself, calculated as

$$\nu = -\frac{\epsilon_{trans}}{\epsilon_{axial}}.$$

In the field of microstructure design, a single material can be made to have very different properties by designing a complex geometry, and we can think of this periodic structural unit as a new material. In general, the Poisson's ratio of such material is not constant and varies with strain and the initial geometry parameters, and the researchers usually adopt infinitesimally small strains to calculate the Poisson's ratio for a given state.

While the unit shapes of our auxetic structures are irregular, they always rotate around the vertices of the anchor frame during the deploying process. Therefore, the overall negative Poisson's ratio property of the structure is closely related to the shape of the anchor frame.

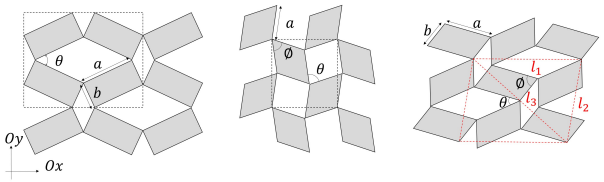

Figure 10: Negative Poisson's ratio calculations for different types of rotating structures.

According to [1, 6, 7], it is known that the negative Poisson's ratio of a square rotating structure is consistently -1. Additionally, as shown in Figure 10, the formulas for calculating the negative Poisson's ratio values of rotating (semi-)rigid structures with anchor frames in the shapes of a rectangle, rhombus, and parallelogram are as follows:

Rectangle type I:

$$\nu_{xy} = (\nu_{yx})^{-1} = \frac{a^2\sin^2(\frac{\theta}{2}) - b^2\cos^2(\frac{\theta}{2})}{a^2\cos^2(\frac{\theta}{2}) - b^2\sin^2(\frac{\theta}{2})} \tag{9}$$

Rhombus type α:

$$\nu_{xy} = (\nu_{yx})^{-1} = \frac{\sin(\frac{\theta-\phi}{2})\sin(\frac{\theta+\phi}{2})}{\cos(\frac{\theta-\phi}{2})\cos(\frac{\theta+\phi}{2})} \tag{10}$$

$$= \tan(\frac{\theta-\phi}{2})\tan(\frac{\theta+\phi}{2}) \tag{11}$$

Parallelogram type I α:

$$\nu_{xy} = (\nu_{yx})^{-1} = \frac{(a^2-b^2)(l_2^2l_1^2-l_2^4-A^2)\sin(\theta)+2abl_2^2(l_2^2+l_1^2-l_3^2)\sin(\theta+\phi)+2ab\cos(\theta)\sin(\phi)(l_3^2l_2^2-A^2)}{[(a^2-b^2)\sin(\theta)+2ab\cos(\theta)\sin(\phi)]A^2} \tag{12}$$

These rotating structures have the property of "contraction-expansion-contraction", and will start contracting when the rotation reaches a certain angle, e.g., the square structure starts contracting when the cell rotates more than 45 degrees, while its Poisson's ratio is always -1. The rectangular structure starts contracting after an angle greater than 45°, and its Poisson's ratio changes abruptly, i.e., jumps from negative to positive.

Compared to traditional work that focuses on exploring the relationship between material structure and negative Poisson's ratio, this paper places greater emphasis on the

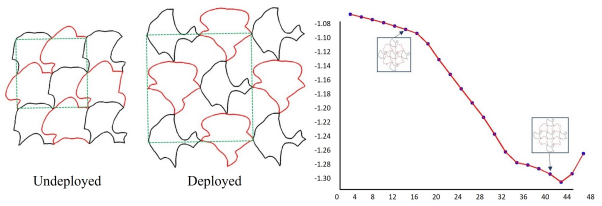

Figure 11: Negative Poisson's ratio of our structure during deploying.

utilization of specific negative Poisson's ratio properties. In this paper, different requirements can be met by choosing a specific anchor frame template, such as restricting the anchor frame to be a square to achieve a constant negative Poisson's ratio.

Additionally, our structures are constrained by the boundary correspondence problem, as a result, we investigates the structural properties during the "contract-expand" phase, specifically with a rotation angle of 45°.

We also calculates the strain values of the structure at both the initial state and a certain moment during the deploying process. The visual results, as shown in Figure 11, indicate that the absolute value of the Poisson's ratio of this structure continues to increase during the rotation process and then begins to decrease at approximately 45 degrees, consistent with the these structures with regular units.

5. Results and Discussions

We implemented our method and tested it on an Intel Core i7-11700F CPU @ 2.5 GHz and 16 GB RAM. We used a filtered database of about 200 shapes based on [51] to generate suitable dihedral Escher tessellation for a single input pattern.

Performance analysis. When given a single shape as input, the algorithm [51] takes at least 20 minutes to generate a dihedral Escher tessellation. While with dihedral shapes, our algorithm takes an average of 13 seconds to generate an auxetic dihedral Escher tessellation. The majority of this time is consumed in the two stages of deployability optimization: frame-deployability optimization and contour-deployability optimization. The former, which does not require any iteration, typically takes 7 seconds, while the latter involves iterative computation of the coordinates of the points, reaching $O(n^2)$ in the worst case and taking 1 second on average.

Table 1: Statistics of the results. Frame types, FDD, λ and E_{sim} of shape merging, CDD and total time for optimization are listed, respectively.

Input	Frame	FDD	λ	E_{sim}	CDD	Time
Swan&fish	parall.	0.112	0.45	0.269	0.161	18.2s
Fish&boat	rhombus	0.078	0.5	0.181	0.608	18.6s
Eagle&bird	parall.	0.070	0.6	0.114	0.236	14.3s
Duck&flower	parall.	0.102	0.35	0.186	0.076	15.5s
Bird&flower	square	0.035	0.55	0.072	0.217	14.6s
Two birds I	parall.	0.018	0.8	0.103	0.565	19.9s
Two birds II	rhombus	0.070	0.55	0.121	0.363	15.1s
Bird&bat	parall.	0.069	0.3	0.146	0.416	19.6s

Dihedral tessellation comparison. In contrast to traditional Escher dihedral tessellations, our auxetic tessellations adhere to stronger constraints, significantly increasing the challenge of preserving the meaning of the dual shapes. As indicated in the Figure 12, the first row displays the results of optimizing hand-drawn tessellations of Escher into auxetic structures. The subsequent three rows showcase the results of optimizing tessellations generated from a single input pattern. Statistical data for results in this paper are listed in Table 1. It is evident that auxetic tessellations, to some extent, compromise the recognizability of geometric features. Therefore, we utilized AI drawing tools such as Runway and Stable Diffusion to assist us in designing textures, aiming to enhance both the aesthetic appeal and recognizability of the deployable tessellations.

Fabricated results. Our deployable structures can be designed at various scales for application in diverse decorative scenes. This includes small-scale deployable structures that can be unfolded to fit decorative surfaces in three-dimensional space, such as artistic lampshades, and large-scale deployable structures that can be prefabricated and assembled from shape templates. The latter is suitable for application on large-scale artistic curved surfaces, such as screens, windows, and other structures. To accommodate these different scales, we have designed various joints tailored for specific results.

For large-scale fabrication, a ring structure is added to each unit at the position of the rotation axis. Since there will be four joints stacked together at the same place, the

two ring structures come with snaps, which should not be more than $1/2$ of the height of the unit. After fabricating by 3D printing, each unit will be placed in the same state as when it was deployed to allow for the combination of joints. After all are assembled, the entire structure can be easily contracted, as shown in Figure 13.

For small-scale structures, we can generally fabricate them directly through 3D printing or laser cutting, as illustrated in Figure 14 and right column in Figure 3. Instead of joints, the units are connected with each other directly, and the rotational movements of the joints can be accomplished with the help of the elasticity and toughness of the materials themselves, such as PLA and leather.

However, this can lead to stress concentrations in the connecting parts of the structure, resulting in material fracture or fatigue damage, as shown on the left side of Figure 15. There is a need to occasionally increase the thickness of the joints to ensure that the material can withstand numerous "contraction-expansion" processes. However, this solution introduces another challenge: when the connection is excessively thick and the material is soft, the concentrated stresses can cause the connection to warp out of plane. This problem is particularly evident in the work of this paper. Upon observing the comparison in Figure 15, traditional rotating (semi-)rigid structures exhibit regular contours of units, concentrating stresses only in the connected parts. In contrast, the shape units designed in this paper lead to stress dispersion to the other weak areas on the contour, resulting in the outward buckling of the weak areas. This not only significantly increases the difficulty of driving the deploying of the structure, but also leads to serious failure to fully deploy the structure.

The UI tools provided in this paper can be helpful in addressing this challenge. By simulating the forces on the structure, users can manually thicken the weak parts using UI. After the modifications, the system will perform a reevaluation to ensure the deployability of the results.

6. Conclusion

In conclusion, our study focuses on enhancing the aesthetics and deployability of rotating auxetic structures. We propose a deployability optimization algorithm that incorporates meaningful contours and Escher tessellations to address the challenges of preserving rotational degrees of freedom while ensuring deployability. Our algorithm is versatile, capable of handling existing tessellations and single input shapes, resulting in manufacturable products with practical utility.

Our contributions encompass the framework for deforming dihedral shapes into auxetic tessellations, the deployability metric function, and the integration of aesthetics with rotating (semi-)rigid structures. We believe that this work represents an effort to unlock new design possibilities and applications in both artistic and practical domains, thereby advancing the field of deployable structures.

Our method does have limitations. While our auxetic tessellations boast interesting and richly meaningful contours compared to the rotating (semi-)rigid structures of regular geometric units, we acknowledge that we sacrifice a portion of the range of rotation. Moreover, in contrast to triangular rotating structure of [11], our quadrilaterals rotating rigid structures exhibit a significantly lower degree of rotational freedom and a reduced ability to approximate the curvature of surfaces. This limitation arises from the structural difference: in triangular structure, six units form a ring, allowing a part of the units to rotate when another part is fixed. In contrast, in quadrilaterals, when any unit undergoes a rotation, the entire structure theoretically have to rotate simultaneously. Thus, relying on the properties of our structure, we can only approximate a developable surface or, relying on the elasticity of the material, approximate some surfaces of lower curvature. Additionally, our method still requires manual optimization of non-adjacent edges, incurring significant manual effort despite preserving features more effectively. Due to the deployability constraint, we impose stricter requirements on the position of anchor points (i.e. the arrangement position of the dihedral patterns), resulting in a smaller solution space compared to traditional Escher dihedral tessellations. Consequently, we lose more meaning of the contour, necessitating a greater reliance on texture.

One of the most intuitive directions for future work is to enhance the algorithm's capability to handle obstructing non-adjacent edges. Upon detecting a collision, the algorithm could iteratively move the collision point and its surrounding points a certain distance in the opposite direction, similar to how we optimized adjacent edges, thus automatically separating the non-adjacent edges. Another avenue for future work involves designing shapes

for the unfolded gaps to make them more interesting. Currently, each void space consists of two identical pairs of edges, limiting the variety of shapes that can be accommodated. Exploring innovative designs for these gaps could broaden the aesthetic possibilities of the algorithm.

Acknowledgement

We thank all the anonymous reviewers for their valuable comments and constructive suggestions. This work is supported by the grant No.61972232 from National Natural Science Foundation of China (NSFC) and the Key Research and Development Plan of Shandong Province of China (No.2020ZLYS01).

References

[1] J. N. Grima, K. E. Evans, Auxetic behavior from rotating squares, Journal of materials science letters 19 (2000) 1563–1565.

[2] J. N. Grima, A. Alderson, K. E. Evans, Negative poisson's ratios from rotating rectangles, Comput. Methods Sci. Technol 10 (2) (2004) 137–145.

[3] J. N. Grima, R. Gatt, A. Alderson, K. E. Evans, On the auxetic properties of 'rotating rectangles' with different connectivity, Journal of the Physical Society of Japan 74 (10) (2005) 2866–2867.

[4] J. N. Grima, K. E. Evans, Auxetic behavior from rotating triangles, Journal of materials science 41 (10) (2006) 3193–3196.

[5] J. N. Grima, V. Zammit, R. Gatt, A. Alderson, K. Evans, Auxetic behaviour from rotating semi-rigid units, physica status solidi (b) 244 (3) (2007) 866–882.

[6] J. N. Grima, P.-S. Farrugia, R. Gatt, D. Attard, On the auxetic properties of rotating rhombi and parallelograms: A preliminary investigation, physica status solidi (b) 245 (3) (2008) 521–529.

[7] D. Attard, E. Manicaro, J. N. Grima, On rotating rigid parallelograms and their potential for exhibiting auxetic behaviour, physica status solidi (b) 246 (9) (2009) 2033–2044.

[8] J. N. Grima, E. Manicaro, D. Attard, Auxetic behaviour from connected different-sized squares and rectangles, Proceedings of the royal society A: mathematical, physical and engineering sciences 467 (2126) (2011) 439–458.

[9] G. P. Choi, L. H. Dudte, L. Mahadevan, Compact reconfigurable kirigami, Physical Review Research 3 (4) (2021) 043030.

[10] K. Warisaya, H. Hamanaka, A. Tokolo, T. Tachi, Auxetic structures based on rhombic tiling, in: International Design Engineering Technical Conferences and Computers and Information in Engineering Conference, Vol. 85451, American Society of Mechanical Engineers, 2021, p. V08BT08A031.

[11] M. Konaković, K. Crane, B. Deng, S. Bouaziz, D. Piker, M. Pauly, Beyond developable: computational design and fabrication with auxetic materials, ACM Transactions on Graphics (TOG) 35 (4) (2016) 1–11.

[12] M. Konaković-Luković, J. Panetta, K. Crane, M. Pauly, Rapid deployment of curved surfaces via programmable auxetics, ACM Transactions on Graphics (TOG) 37 (4) (2018) 1–13.

[13] C. Jiang, F. Rist, H. Wang, J. Wallner, H. Pottmann, Shape-morphing mechanical metamaterials, Computer-Aided Design 143 (2022) 103146.

[14] A. Rafsanjani, D. Pasini, Bistable auxetic mechanical metamaterials inspired by ancient geometric motifs, Extreme Mechanics Letters 9 (2016) 291–296.

[15] T. Chen, J. Panetta, M. Schnaubelt, M. Pauly, Bistable auxetic surface structures, ACM Transactions on Graphics (TOG) 40 (4) (2021) 1–9.

[16] L. J. Gibson, M. F. Ashby, G. Schajer, C. Robertson, The mechanics of two-dimensional cellular materials, Proceedings of the Royal Society of London. A. Mathematical and Physical Sciences 382 (1782) (1982) 25–42.

[17] R. Lakes, Deformation mechanisms in negative poisson's ratio materials: structural aspects, Journal of materials science 26 (1991) 2287–2292.

[18] D. Prall, R. Lakes, Properties of a chiral honeycomb with a poisson's ratio of—1, International Journal of Mechanical Sciences 39 (3) (1997) 305–314.

[19] J. N. Grima, R. Gatt, Perforated sheets exhibiting negative poisson's ratios, Advanced engineering materials 12 (6) (2010) 460–464.

[20] D. Attard, J. N. Grima, A three-dimensional rotating rigid units network exhibiting negative poisson's ratios, physica status solidi (b) 249 (7) (2012) 1330–1338.

[21] Y. Li, Q. Zhang, Y. Hong, J. Yin, 3d transformable modular kirigami based programmable metamaterials, Advanced Functional Materials 31 (43) (2021) 2105641.

[22] R. Gatt, L. Mizzi, J. I. Azzopardi, K. M. Azzopardi, D. Attard, A. Casha, J. Briffa, J. N. Grima, Hierarchical auxetic mechanical metamaterials, Scientific reports 5 (1) (2015) 8395.

[23] J. N. Grima, R. Gatt, B. Ellul, E. Chetcuti, Auxetic behaviour in non-crystalline materials having star or triangular shaped perforations, Journal of Non-Crystalline Solids 356 (37-40) (2010) 1980–1987.

[24] A. Slann, W. White, F. Scarpa, K. Boba, I. Farrow, Cellular plates with auxetic rectangular perforations, physica status solidi (b) 252 (7) (2015) 1533–1539.

[25] N. Pagliocca, K. Z. Uddin, I. A. Anni, C. Shen, G. Youssef, B. Koohbor, Flexible planar metamaterials with tunable poisson's ratios, Materials & Design 215 (2022) 110446.

[26] M. Morvaridi, G. Carta, F. Bosia, A. S. Gliozzi, N. M. Pugno, D. Misseroni, M. Brun, Hierarchical auxetic and isotropic porous medium with extremely negative poisson's ratio, Extreme Mechanics Letters 48 (2021) 101405.

[27] L. Mizzi, K. M. Azzopardi, D. Attard, J. N. Grima, R. Gatt, Auxetic metamaterials exhibiting giant negative poisson's ratios, physica status solidi (RRL)–Rapid Research Letters 9 (7) (2015) 425–430.

[28] S. Shan, S. H. Kang, Z. Zhao, L. Fang, K. Bertoldi, Design of planar isotropic negative poisson's ratio structures, Extreme Mechanics Letters 4 (2015) 96–102.

[29] C. Schüller, R. Poranne, O. Sorkine-Hornung, Shape representation by zippables, ACM Transactions on Graphics (TOG) 37 (4) (2018) 1–13.

[30] Y. Ren, J. Panetta, T. Chen, F. Isvoranu, S. Poincloux, C. Brandt, A. Martin, M. Pauly, 3d weaving with curved ribbons, ACM Transactions on Graphics 40 (ARTICLE) (2021) 127.

[31] J. Panetta, M. Konaković-Luković, F. Isvoranu, E. Bouleau, M. Pauly, X-shells: A new class of deployable beam structures, ACM Transactions on Graphics (TOG) 38 (4) (2019) 1–15.

[32] S. Pillwein, K. Leimer, M. Birsak, P. Musialski, On elastic geodesic grids and their planar to spatial deployment, arXiv preprint arXiv:2007.00201 (2020).

[33] S. Pillwein, J. Kübert, F. Rist, P. Musialski, Design and fabrication of multi-patch elastic geodesic grid structures, Computers & Graphics 98 (2021) 218–230.

[34] S. Pillwein, P. Musialski, Generalized deployable elastic geodesic grids, ACM Transactions on Graphics (TOG) 40 (6) (2021) 1–15.

[35] C. Jiang, C. Wang, X. Tellier, J. Wallner, H. Pottmann, Planar panels and planar supporting beams in architectural structures, ACM Transactions on Graphics 42 (2) (2022) 1–17.

[36] D. LIU, D. PELLIS, Y.-C. CHIANG, F. RIST, J. WALLNER, H. POTTMANN, Deployable strip structures, ACM Trans. Graph 42 (4) (2023).

[37] C. Zheng, T. Sun, X. Chen, Deployable 3d linkages with collision avoidance., in: Symposium on Computer Animation, 2016, pp. 179–188.

[38] Y. Ren, U. Kusupati, J. Panetta, F. Isvoranu, D. Pellis, T. Chen, M. Pauly, Umbrella meshes: elastic mechanisms for freeform shape deployment, ACM Transactions on Graphics 41 (ARTICLE) (2022) 1–15.

[39] D. Schattschneider, et al., Visions of symmetry: Notebooks, periodic drawings, and related work of MC Escher, Vol. 8, WH Freeman New York, 1990.

[40] A. W. Dress, The 37 combinatorial types of regular\heaven and hell" patterns in the euclidean plane, MC Escher: Art and science (1986) 35–43.

[41] B. Grünbaum, G. C. Shephard, Tilings and patterns, Courier Dover Publications, 1987.

[42] C. S. Kaplan, D. H. Salesin, Escherization, in: Proceedings of the 27th annual conference on Computer graphics and interactive techniques, 2000, pp. 499–510.

[43] C. Kaplan, D. Salesin, Dihedral escherization, in: Proceedings of Graphics Interface 2004, GI 2004, Canadian Human-Computer Communications Society, School of Computer Science, University of Waterloo, Waterloo, Ontario, Canada, 2004, pp. 255–262.

[44] H. Koizumi, K. Sugihara, Maximum eigenvalue problem for escherization, Graphs and Combinatorics 27 (2011) 431–439.

[45] S. Ono, M. Kisanuki, H. Machii, K. Mizuno, Creation support for escher-like tiling patterns by interactive genetic algorithms, in: SIGGRAPH Asia 2014 Posters, 2014, pp. 1–1.

[46] Y. Nagata, S. Imahori, Escherization with large deformations based on as-rigid-as-possible shape modeling, ACM Transactions on Graphics (TOG) 41 (2) (2021) 1–16.

[47] K. Sugihara, Computer-aided generation of escher-like sky and water tiling patterns, Journal of Mathematics and the Arts 3 (4) (2009) 195–207.

[48] S.-S. Lin, C. C. Morace, C.-H. Lin, L.-F. Hsu, T.-Y. Lee, Generation of escher arts with dual perception, IEEE transactions on visualization and computer graphics 24 (2) (2017) 1103–1113.

[49] J. Yen, C. Séquin, Escher sphere construction kit, in: Proceedings of the 2001 symposium on Interactive 3D graphics, 2001, pp. 95–98.

[50] M. Howison, C. H. Séquin, Cad tools for creating space-filing 3d escher tiles, Computer-Aided Design and Applications 6 (6) (2009) 737–748.

[51] X. Liu, L. Lu, A. Sharf, X. Yan, D. Lischinski, C. Tu, Fabricable dihedral escher tessellations, Computer-Aided Design 127 (2020) 102853.

[52] T. Igarashi, T. Moscovich, J. F. Hughes, As-rigid-as-possible shape manipulation, ACM transactions on Graphics (TOG) 24 (3) (2005) 1134–1141.

[53] N. Alajlan, M. S. Kamel, G. H. Freeman, Geometry-based image retrieval in binary image databases, IEEE transactions on pattern analysis and machine intelligence 30 (6) (2008) 1003–1013.

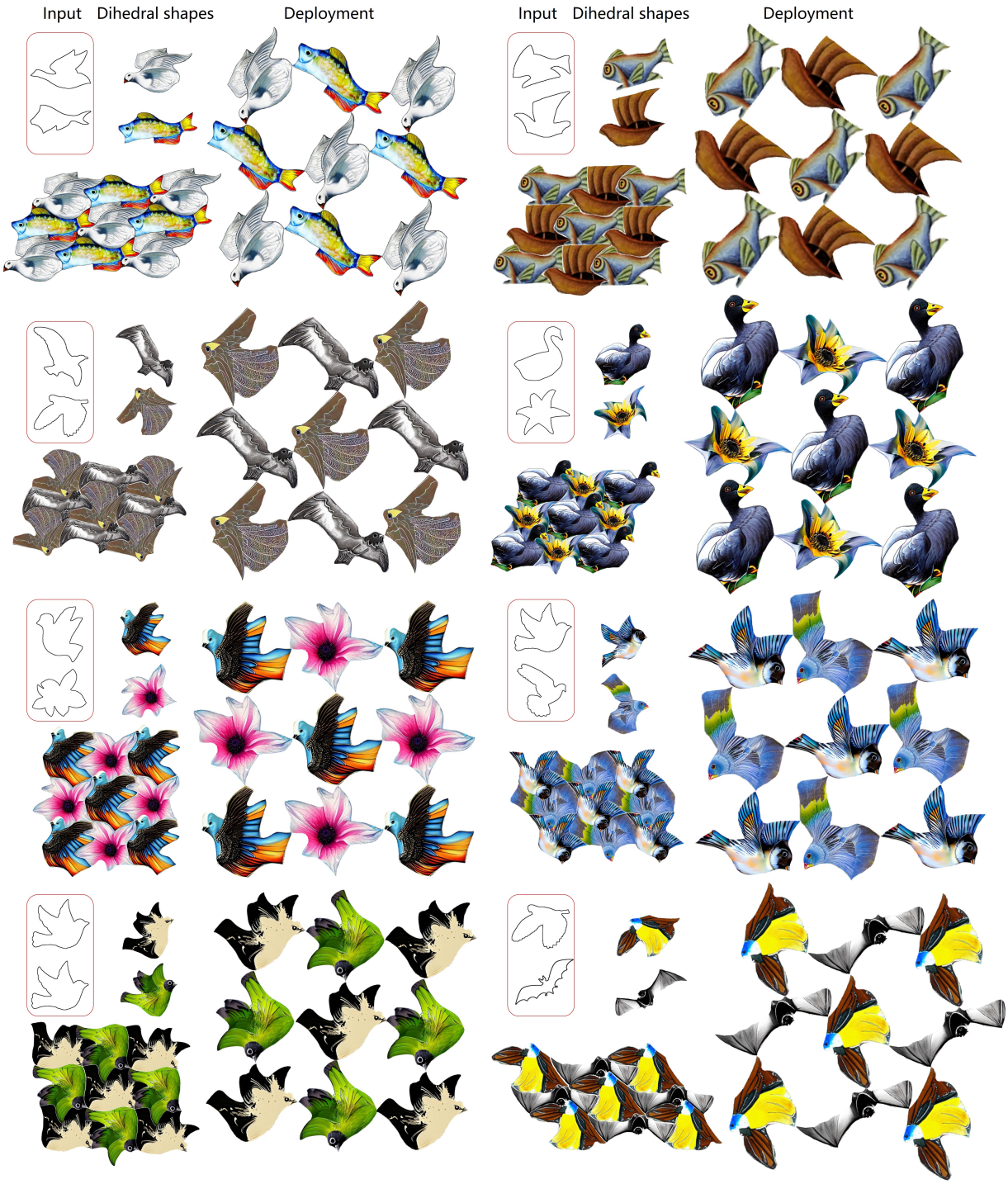

Figure 12: Auxetic dihedral Escher tessellations. The top row is obtained through deployability optimization on Escher's hand-drawn artwork, and the other three rows are based on the newly generated dual-shape tessellations.

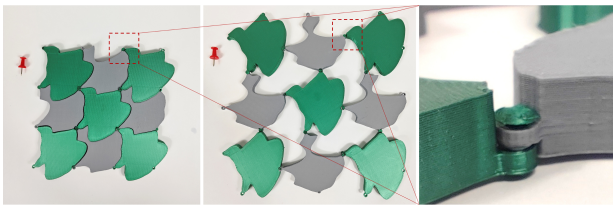

Figure 13: Assemblable joint design for large-scale manufacturing.

Figure 14: Auxetic leather tape fabricated through laser cutting.

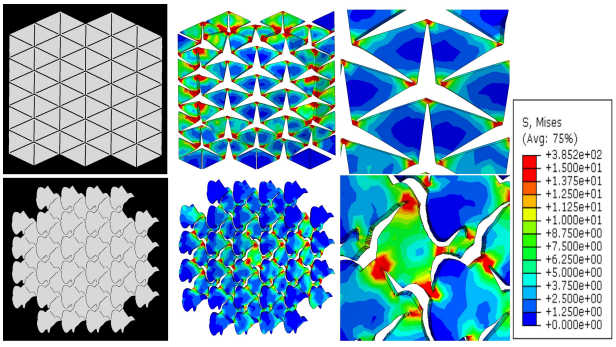

Figure 15: Stress analysis for triangular rotating (semi-)rigid structure and the structure proposed in this paper. It can be observed that the stress in the triangular structure mainly concentrates at the connections, while in our structure, stress is not only concentrated at the connection points but also extends to the tail of ”fish”, even surpassing the connection region at the tail. This undoubtedly leads to deformation in the structure during the deploying process.